INTERNATIONAL JOURNAL FOR NUMERICAL METHODS IN FLUIDS
Int. J. Numer. Meth. Fluids 2004; **45**:1009–1023 (DOI: 10.1002/fld.736)

Modelling of a single drop impact onto liquid film using particle method

Heng Xie*,†, Seiichi Koshizuka and Yoshiaki Oka

Nuclear Engineering Research Laboratory, The University of Tokyo, Japan

SUMMARY

The process of single liquid drop impact on thin liquid surface is numerically simulated with moving particle semi-implicit method. The mathematical model involves gravity, viscosity and surface tension. The model is validated by the simulation of the experimental cases. It is found that the dynamic processes after impact are sensitive to the liquid pool depth and the initial drop velocity. In the cases that the initial drop velocity is low, the drop will be merged with the liquid pool and no big splash is seen. If the initial drop velocity is high enough, the dynamic process depends on the liquid depth. If the liquid film is very thin, a bowl-shaped thin crown is formed immediately after the impact. The total crown subsequently expands outward and breaks into many tiny droplets. When the thickness of the liquid film increases, the direction of the liquid crown becomes normal to the surface and the crown propagates outward. It is also found that the radius of the crown is described by a square function of time: $r_C = [c(t - t_0)]^{0.5}$. When the liquid film is thick enough, a crown and a deep cavity inside it are formed shortly after the impact. The bottom of the cavity is initially oblate and then the base grows downward to form a sharp corner and subsequently the corner moves downward. Copyright © 2004 John Wiley & Sons, Ltd.

KEY WORDS: MPS method; drop impact; liquid surface; numerical simulation

1. INTRODUCTION

The characteristics of liquid droplet impinging on surface are of great importance in a variety of fields. For example, high-speed impacts with solids can cause severe erosion in steam turbines. The splashing of raindrops plays an important role in soil erosion and in the dispersal of seeds and microorganisms. The other engineering application includes spray cooling, spray coating and ink-jet painting. This process can also be encountered in nuclear engineering. In light water reactor (LWR) many phenomena are related to liquid droplet behaviours, such as the mist-annular flow existing in boiling water reactor (BWR) and the dispersed droplet flow in post critical heat flux (CHF) regime. In the former, the mechanism of the droplet impacting on the liquid film attached on the surface of fuel rod will affect the depositions of droplet and subsequently the mass flux and thickness of the liquid film which are key parameters

*Correspondence to: Heng Xie, Nuclear Engineering Research Laboratory, The University of Tokyo, 2-22 shirane, shirakata, Tokai-mura, Naka-gun, Ibaraki 319-1188, Japan.
†E-mail: xie@utnl.jp

Published online 4 May 2004

Received 3 June 2003
Revised 7 March 2004

of dry-out phenomena. In the latter, direct contact between liquid droplets and wall has an important contribution to the total heat transfer [1, 2].

The characteristics of the droplet/surface interactions depend upon the properties of the droplet, the impacted surface, impact velocity, impact angle, geometry, and the medium through which the droplet traverses prior to impact. The fluid flow associated with it is rather complicated and not understood in detail despite many investigations since more than one hundred years ago [3]. Rein reviewed it some years ago [4].

An important distinction made for liquid droplet/surface interaction is the type of impacted surface. The target surface can be either a solid or a liquid surface. Depending on the type, the dynamics process of the impacting can be vastly different. The fluid mechanics of droplet collision with a solid surface has been studied in great detail by the experimental [5–10] and numerical simulation method [11–15]. The research on the impact of a liquid droplet with a liquid surface is comparably rare. It is found that qualitatively different behaviours and phenomena can occur under different condition: the drop coalescence with the liquid surface, splashing by creating a crown, a so-called Worthington jet or a vortex, droplet rebound, etc. In several cases, one or more bubbles can be entrained by the drop impact. The entrained bubbles are thought as the reason of the rejected jet [16, 17]. This phenomenon does not occur in the cases of shallow liquid surface [18]. Hobbs and Osheroff [19] studied the splashing of a drop after impacting on the liquid pool with different depths using the photographs taken by a high-speed camera. They found that the phenomena had close relation to the depth of the target liquid pool. In their experiment, it was found that no jet drops were produced for the pool depth less than 3 mm. Clearer photos were gotten by Macklin and Hobbs [20] by high-speed movies. They also explained the phenomena by the interaction of the subsurface cavity with the solid surface beneath the liquid. Wang and Chen [21] experimentally studied the drop impingement onto liquid films with thickness of the order of 1 mm using the glycerol–water solution. The thickness of liquid film is varied to study the effect of it. The effect of viscosity is also studied by changing the proportion of glycerol to water. In Manzello and Yang's paper [22], the depth of the impacted liquid pool was varied from 2 to 25 mm to show the role of the depth of impacted liquid surface. Weiss and Yarin [18] used a boundary-integral method to numerically simulate the single drop impact onto liquid film. In their paper, the potential flow is assumed to build the model.

To simulate large deformation of free surface like the drop impact, particle method has natural advantage because in this method it is not necessary to use artificial method to track the free surface and the interfaces are always clear. The numerical diffusion can also be avoided because the convection is directly calculated by the motion of particles. In present study, moving-particle semi-implicit method (MPS) is employed to simulate dynamics process of droplet impact on thin liquid surface. The typical cases in References [21, 22] are chosen to simulate. The calculated results are compared with the experimental results to verify the model. The effects of depth of liquid are also numerically studied and analysed.

2. MATHEMATIC MODEL

2.1. Governing equations

Mass and momentum equations for incompressible flows are shown as follow:

$$\nabla \cdot \mathbf{u} = 0 \tag{1}$$

$$\rho\frac{D\mathbf{u}}{Dt} = -\nabla P + \mu\nabla^2\mathbf{u} + \rho g + \sigma k\delta\mathbf{n} \tag{2}$$

where ρ is the density, $\mathbf{u}$ is velocity, t is time, P is pressure, μ is viscosity coefficient, g is the acceleration due to gravity, σ is surface tension coefficient, k is the curvature of the surface, δ is the delta function, $\mathbf{n}$ is the unit vector normal to the interface.

These governing equations involve differential operators, such as gradient and Laplacian. The method to discretize these operators is shown in the next subsection. The calculation of convection terms is not necessary since the MPS method is fully Lagrangian. Thus, numerical diffusion does not occur.

2.2. MPS method

Since the method has been introduced in many published paper, it is described in brief here. The detail of the model and the algorithm can be seen from References [23–26].

In the MPS method a particle interacts with others in its vicinity covered with a weight function $w(r)$, where r is the distance between two particles (Figure 1). In this study, the following function is employed:

$$w(r) = \begin{cases} \dfrac{r_e}{r} - 1 & (r < r_e) \\ 0 & (r > r_e) \end{cases} \tag{3}$$

Since the area that is covered with this weight function is bounded, a particle interacts with a finite number of neighbouring particles. The radius of the interaction area is determined by

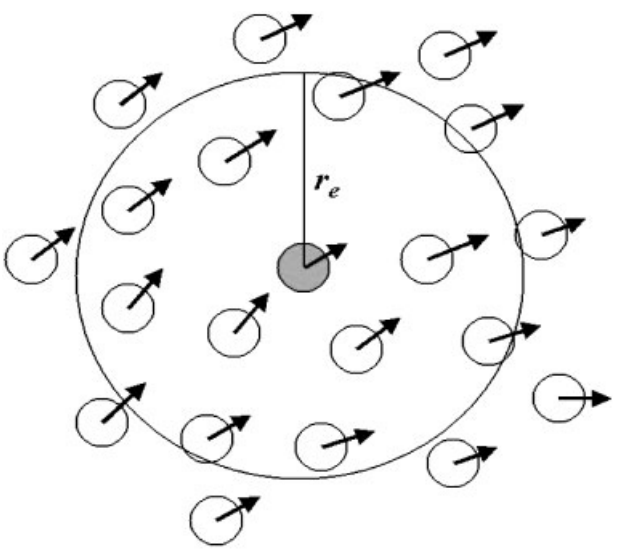

Figure 1. Particle interaction within weight function.

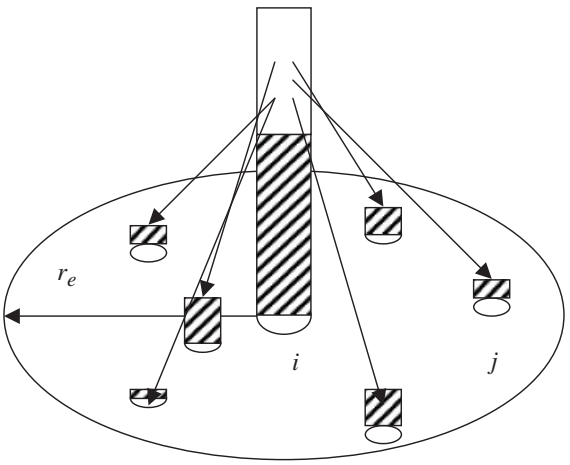

Figure 2. Concept of Laplacian model.

a parameter r_e. The particle number density at co-ordinates $\mathbf{r}_i$ is defined by

$$\langle n \rangle_i = \sum_j w(|\mathbf{r}_j - \mathbf{r}_i|) \tag{4}$$

A gradient vector between two particles i and j possessing scalar quantities ϕ_i and ϕ_j at co-ordinates $\mathbf{r}_i$ and $\mathbf{r}_j$ is simply defined by $(\phi_j - \phi_i)(\mathbf{r}_j - \mathbf{r}_i)/|\mathbf{r}_j - \mathbf{r}_i|^2$. The gradient vector at the particle i is given as the weighted average of these gradient vectors.

$$\langle \nabla \phi \rangle_i = \frac{d}{n^0} \sum_{j \neq i} \left[\frac{\phi_j - \phi_i}{|\mathbf{r}_j - \mathbf{r}_i|^2} (\mathbf{r}_j - \mathbf{r}_i) w(|\mathbf{r}_j - \mathbf{r}_i|) \right] \tag{5}$$

where d is the number of space dimensions and n^0 is the particle number density.

Laplacian is an operator representing diffusion. In the MPS method, diffusion is modelled by distribution of a quantity from a particle to its neighbouring particles by use of the weight function as shown in Figure 2:

$$\langle \nabla^2 \phi \rangle_i = \frac{2d}{n^0 \lambda} \sum_{j \neq i} [(\phi_j - \phi_i) w(|\mathbf{r}_j - \mathbf{r}_i|)] \tag{6}$$

where λ is a parameter by which the variance increase is equal to that of the analytical solution:

$$\lambda = \frac{\sum_{j \neq i} w(|\mathbf{r}_j - \mathbf{r}_i|) |\mathbf{r}_j - \mathbf{r}_i|^2}{\sum_{j \neq i} w(|\mathbf{r}_j - \mathbf{r}_i|)} \tag{7}$$

Incompressibility is calculated by a semi-implicit algorithm where the pressure field is implicitly solved using Poisson equation, while the other terms are explicitly calculated,

$$\langle \nabla^2 P \rangle_i = -\frac{\rho}{\Delta t^2} \frac{n_i^* - n^0}{n^0} \tag{8}$$

where superscript * stands for a temporal value after explicit calculation step. The source term of Poisson equation is represented by the deviation of the particle number density from the constant value of n^0.

2.3. Discretization of viscosity

In the momentum equation (2), the viscosity term has the form of Laplacian operator. So Equation (6) is adopted for discretization of the viscosity term:

$$\langle \nabla^2 \mathbf{u} \rangle_i = \frac{2d}{n^0 \lambda} \sum_{j \neq i} (\mathbf{u}_j - \mathbf{u}_i) w(|\mathbf{r}_j - \mathbf{r}_i|) \tag{9}$$

The model of the viscosity term is added after the calculation of gravity. An explicit algorithm is employed,

$$\mathbf{u}_i^{**} = \mathbf{u}_i^* + v \langle \nabla^2 \mathbf{u}^* \rangle_i \cdot \mathrm{d}t \tag{10}$$

where $\mathbf{u}^{**}$ is the velocity vector after the calculation of the viscosity term, $\mathbf{u}^*$ is the velocity vector before the calculation of the viscosity term.

The viscous force between the liquid particles on the free surface and the outside air is markedly smaller than that between liquid particles in the bulk phase when the velocity of the airflow on the free surface is not very large. Therefore, the outside air is treated as vacuum and no air particles exist. Then Equation (10) can be also fitted to the liquid particles on the free surface.

To the particles near the solid surface boundary, non-slip boundary condition is applied. The velocity of solid particles is modified to make sure the velocity on solid surface is zero. The scheme of the modification is shown as Figure 3. The velocity on the solid surface $\mathbf{u}_s$ is obtained by the linear interpolation of the velocity of the nearest liquid particle $\mathbf{u}_i$ and solid particle $\mathbf{u}_j$ and always keeps the value of zero due to the non-slip boundary condition.

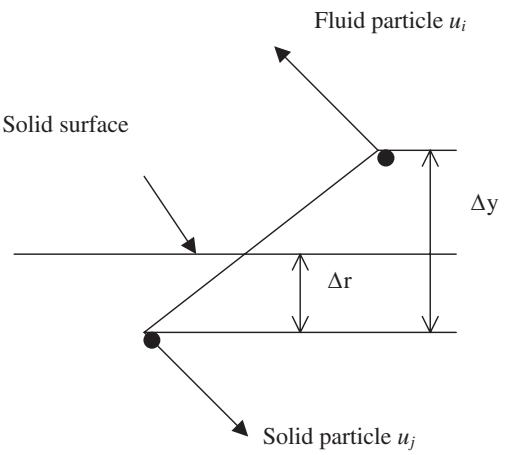

Figure 3. The schematic of the non-slip boundary model.

Therefore, the velocity of a solid particle is modified as

$$\mathbf{u}_j = -\frac{\Delta r}{\Delta y - \Delta r}\mathbf{u}_i \tag{11}$$

where Δr is the distance between the solid surface and the solid particle j; Δy is the distance between the solid particle j and liquid particle i.

It should be mentioned that this modification is only effective in the viscosity term.

2.4. Surface tension model

Surface tension is calculated at the particles on the free surface. We need to obtain curvature κ and unit normal vector $\mathbf{n}$ at such particles (Figure 4). The particle number density is utilized for curvature.

$$\kappa = \frac{2\cos\theta}{r_e^{\mathrm{st}}} \tag{12}$$

$$2\theta = \frac{n_i^{\mathrm{st2}}}{n_0^{\mathrm{st}}}\pi \tag{13}$$

where the weight function used here is special for surface tension,

$$w^{\mathrm{st1}}(r) = \begin{cases} 1, & 0 \leqslant r < r_e^{\mathrm{st}} \\ 0, & r_e^{\mathrm{st}} \leqslant r \end{cases} \tag{14}$$

$$w^{\mathrm{st2}}(r) = \begin{cases} 1, & 0 \leqslant r < r_e^{\mathrm{st}} \text{ and } n_j^{\mathrm{st1}} > n_i^{\mathrm{st1}} \\ 0, & \text{otherwise} \end{cases} \tag{15}$$

where subscript i indicate the calculated particle and j indicate its neighbour particle. r_e^{st} is the parameter that determines the neighbour in the calculation of surface tension. Particle number density n_i^{st1} is calculated by using Equation (14) at first, and n_i^{st2} is then obtained by using Equation (15).

In Equation (13), a flat surface ($2\theta = \pi$) is assumed to be $n_i^{\mathrm{st2}} = n_0^{\mathrm{st}}$, which is estimated in advance in the initial particle configuration. Acute angles are obtained where $n_i^{\mathrm{st2}} < n_0^{\mathrm{st}}$, while obtuse angles are obtained where $n_i^{\mathrm{st2}} > n_0^{\mathrm{st}}$.

The unit normal vector is also calculated by utilizing the particle number density. Particle number densities at four positions near particle i are evaluated, $n_i^{\pm x}(\mathbf{r}_i \pm l_0\mathbf{n}_x)$ and $n_i^{\pm y}(\mathbf{r}_i \pm l_0\mathbf{n}_y)$ where $\mathbf{n}_x$ and $\mathbf{n}_y$ are unit vectors in x and y directions, respectively and l_0 is the initial average distance between particles. The unit normal vector is calculated as

$$\mathbf{a}_i = \frac{n_i^{+x} - n_i^{-x}}{2l_0}\mathbf{n}_x + \frac{n_i^{+y} - n_i^{-y}}{2l_0}\mathbf{n}_y \tag{16}$$

$$\mathbf{n}_i = \frac{\mathbf{a}_i}{|\mathbf{a}_i|} \tag{17}$$

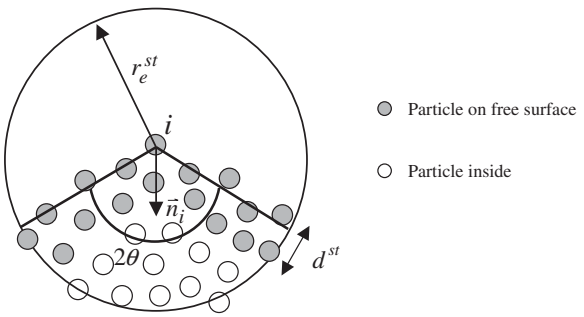

Figure 4. Surface tension model.

Vector $\mathbf{a}_i$ represents gradient of the particle number density around particle i. Smoothing of curvature is sometimes necessary for stability. The curvature κ_i is smoothed by an averaging process among its neighbour particles.

$$\kappa_i = \left(\kappa_i + \sum_{j \neq i} \kappa_j \omega^{\mathrm{st1}}(r_j - r_i) \right) \Big/ 2.0 \tag{18}$$

As shown in Figure 4, free surfaces have a thickness. Thus, we need to divide the calculated surface tension by the normalized thickness of d^{st}/l_0. This model is based on the distribution of the particle number density because it decreases toward the free surface. This idea is similar to the CSF model [27].

The verification of the surface tension model can be seen in Reference [26].

2.5. Gas bubble entrainment

In some experimental results, it was found that gas bubbles were entrained into the liquid pool by the impact. This explains the formation of ejected central jet. But Weiss and Yarin [18] reviewed the previous experimental results and found that this phenomena did not occur in the cases of shallow liquid pool that is the interest of this research. Therefore, the gas bubble model is not included in this paper. The rationality of this hypothesis will be further verified in Section 3.

3. RESULTS AND DISCUSSION

To illustrate the complete progress of droplet splash after impact and verify the model described above, the cases in Wang and Chen's paper [21] are selected as the simulation examples.

In Wang and Chen's experiment, the glycerol-water solutions are used as the working medium and the impacting drop and target liquid are the same fluid. The 'single-shot-flash' photographic technique is used to freeze the instantaneous motion of the impact, and the impinging velocity is measured from the images of the drop during the last 0.1 ms period before it contacts the target liquid surface. The complete sequences of photograph of three

cases in which the liquid film thickness and impact velocity vary are available in the paper. All parameters of drop and target liquid film are also shown in the paper.

The diameter D of the drop is 4.2 mm. The density ρ of the glycerol–water solution used in these three cases is 1200 kg/m^3. The viscosity μ is 0.022 Ns/m^2. The surface tension coefficient σ is 0.0652 N/m. The Ohnesorge number ($Oh = \mu/(\sigma\rho D)^{0.5}$) is 0.0384.

In case A [21, Figure 2], the impact Weber number ($We = \rho U^2 D/\sigma$, where U is the drop velocity before impact) is 381 and the dimensionless film thickness H (the ratio of target liquid film thickness to drop diameter) is 0.05. In case B [21, Figure 3(a)], the dimensionless film thickness H is kept at 0.05 but the impact Weber number is increased to 2010. In case C [21, Figure 3(b)], the impact Weber number is the same as that of case B but the dimensionless film thickness H is increases to 0.5.

The two-dimensional version of the MPS method is used. The co-ordinates normal and parallel to the liquid surface are considered. The calculated results of case A are shown in Figure 5. From the figure, it can be seen that a small rim forms in the contact area between the drop and films immediately after the drop attacks on the liquid film. The particles in the liquid film suffer the impulsive force from the drop and the resistance from the static liquid film. There is no resistance existing in the direction inclined outward. Therefore, the particles move to this direction and a rim forms at the edge of the drop. When more particles in the drop impact on the film, their kinetic energy is reflected by the solid surface. The spreading process begins when the velocity is changed to outward. With the supply of mass and kinetic energy from the drop, the rim expands and propagates outward. A structure looking like the crown is formed. The edge of the rim becomes sharp and its curvature is large which causes strong surface tension that will hold back the expansion of the rim. When the kinetic energy is completely dissipated by the viscosity and surface tension, the crown falls down and merges with the film. The calculated result basically agrees with the experimental result. The main difference between them is that some small drops appear at the edge of the rim in the calculated result but this phenomenon does not occur in the experimental result. The mass of small drops is only a small part of that of the initial drop. It should be mentioned that the thickness of the film on the contact area becomes thicker after the impact due to the mass supply from the drop. This means that the solid surface under the liquid film will not be exposed to air although it is impacted by the drop. This phenomenon perhaps has a special meaning in BWR condition since the liquid film will not be broken due to the impact of drop.

Figure 6 shows the calculated result of case B. Compared to case A, the impact Weber number is increased from 381 to 2010 with keeping the dimensionless film thickness. Similar to Figure 5, a rim forms at the contact area between the drop and the film immediately after impact. At the beginning the rim is slightly tilted backwards at its top in a very short time, then its top becomes straight and subsequently tilts forward. The crown formed in this case is bigger than that in Figure 5 due to the larger impact velocity. The crown breaks up into many smaller drops. The thickness of the film on the contact area also becomes thicker during the complete process. The calculated result agrees with the experimental result.

The calculated result by the MPS method of case C is shown in Figure 7. The only different parameter between cases B and C is the liquid film thickness. The value of dimensionless film thickness H is increased from 0.05 in case B to 0.5 in case C. By comparing Figure 7 and 6, two distinct differences can be observed. One is the shape of the crown formed after impact; the whole crown wall significantly expands outwards as the shape of a bowl in Figure 6 while the crown wall develops approximately normal to the solid surface and looks like a cylinder

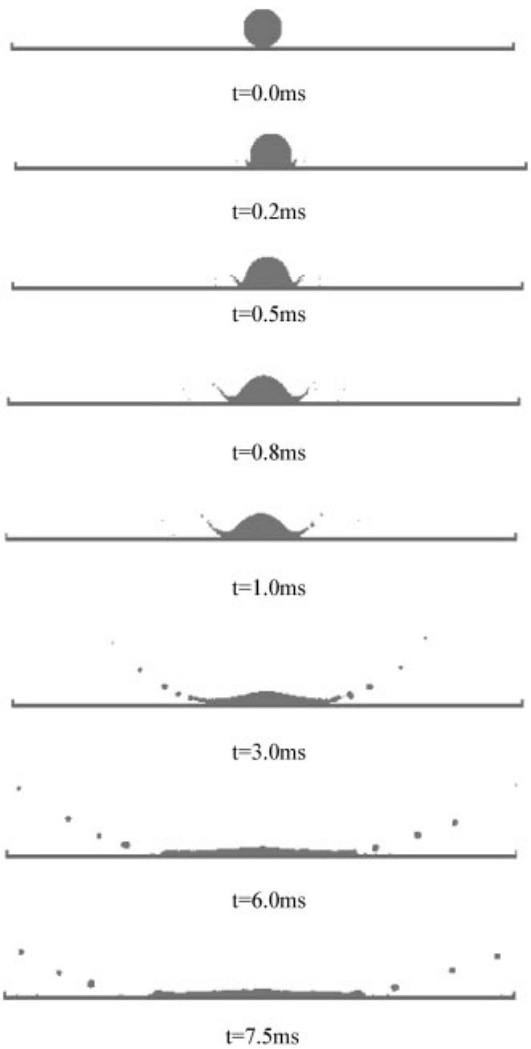

Figure 5. Calculated results of case A.

in Figure 7. The second difference is that the crown totally breaks up into tiny droplets shortly after the impact in Figure 6. But this phenomenon does not occur in Figure 7 in which only several tiny droplets eject from the top of the crown. This can be explained as follows; the liquid film plays a role of buffer. Most of the kinetic energy of the impact drop is absorbed and dissipated by the liquid film. The thicker the liquid film is, the smaller the reflected kinetic energy is. Therefore, the expansion speed of the crown is smaller and the crown does not get enough energy to overcome the surface tension to break up. From the calculated result it can be found that the thickness of the liquid film becomes thinner after impact due to the cavity formed by impact. The calculated result agrees well with the experimental result.

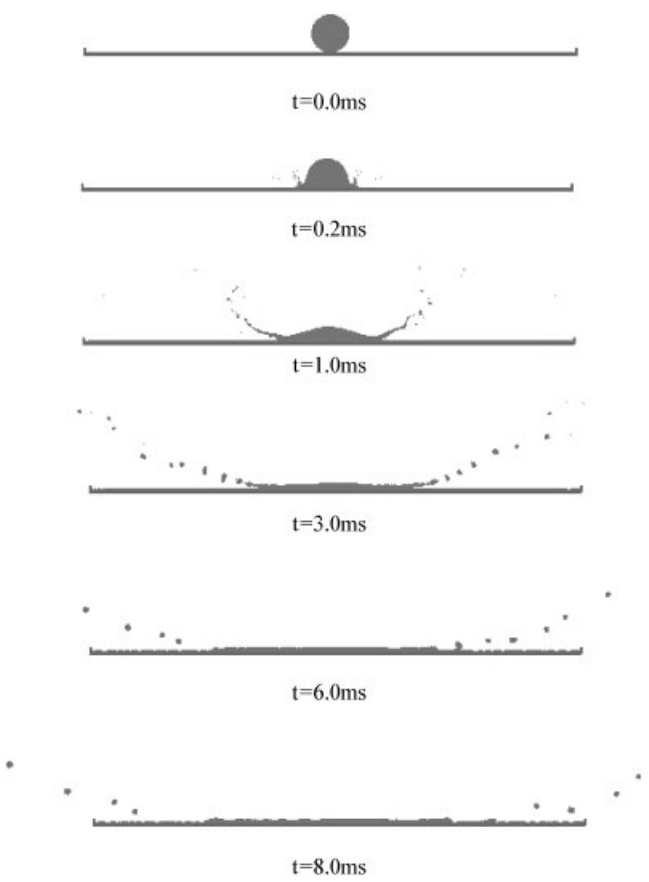

Figure 6. Calculated results of case B.

In Reference [18], it is found that the radius of the crown formed by impact x_c can be very accurately described by a square-root function of time t: $x_c = [c(t - t_0)]^{1/2}$, where c and t_0 are constant. We try to fit the calculated result of the crown in Figure 7 by the same form. The result is shown in Figure 8. The crown width y is fitted by the equation $y = 0.00913(t + 0.4)^{0.5}$ (unit of y is m and unit of t is ms) that shows good agreement.

In the above calculated result and Wang and Chen's experimental photos, the central jet described in References [16, 17] is not found. In Reference [16], it is thought that the central jet is related to the gas bubble entrainment. In the present study the liquid film is very thin, so that it is impossible to entrain a gas bubble. To further verify this idea, two cases in Reference [22] are chosen to simulate. The working medium is water on atmospheric air. The first case is the drop impact on a shallow liquid pool whose depth is 2 mm. The impact Weber number is 202. The calculated results are shown in Figure 9. In the figure, it can be seen that the crown sharp is similar to that in Figure 7. The reason is that the depths of targeted liquid pool are similar in these two cases.

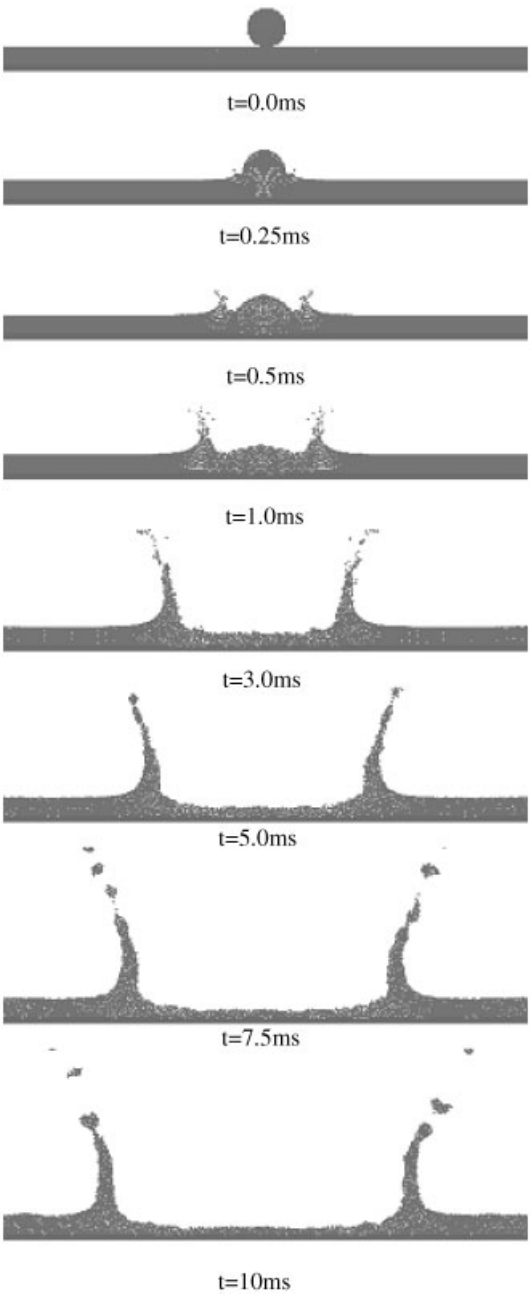

Figure 7. Calculated results of case C.

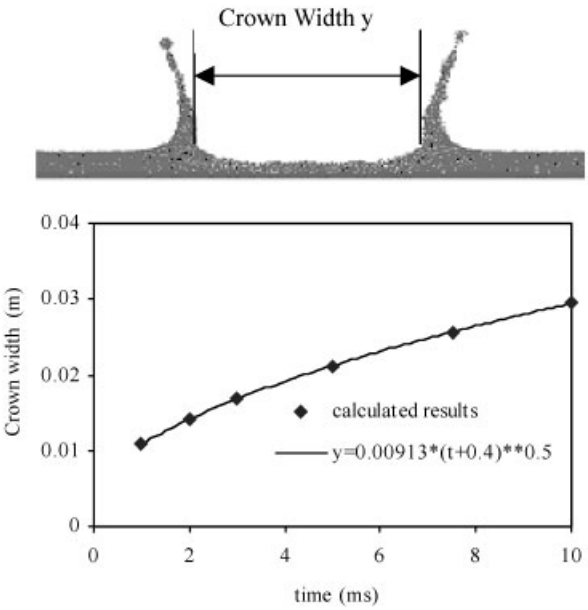

Figure 8. The kinematics of the crown width.

The second case chosen from Reference [22] to simulate is the drop impact on a liquid pool whose depth is 7 mm. The impact Weber number is also 202. The calculated result is shown in Figure 10. The result is obviously different from that of the previous case. Immediately after impact a semicircular crater is formed in the target liquid pool. Then the size of the crater increases and the shape of it changes. The crater becomes oblate and its base grows downward to form a sharp hole. The pictures under the liquid surface cannot be seen in the photos in Manzello and Yang's paper, though similar shapes can be seen in References [16, 17]. In References [16, 17], the sharp hole on the base of the crater causes gas bubble entrainment that is the reason of the rejected central jet. In the present study the rejected jet cannot be simulated since the gas model is not included.

4. CONCLUSION AND FURTHER WORK

In the present study, the process of a single liquid drop impact on thin liquid film is numerically simulated with moving particle semi-implicit (MPS) method. The model is validated by simulating the experiment cases in Wang and Chen's paper and Manzello and Yang's paper. In these cases, the calculated results agree well with the experimental results.

It is found that the dynamic process after impact is sensitive to the thickness of the liquid pool and the initial drop velocity. In the cases that the initial drop velocity is low, the drop merges with the liquid film and no strong splash is observed. The thickness of the film in the area of impact increases due to the mass from the drop. If the initial drop velocity is high enough, the dynamic process after impact depends on the thickness of the liquid film. If the

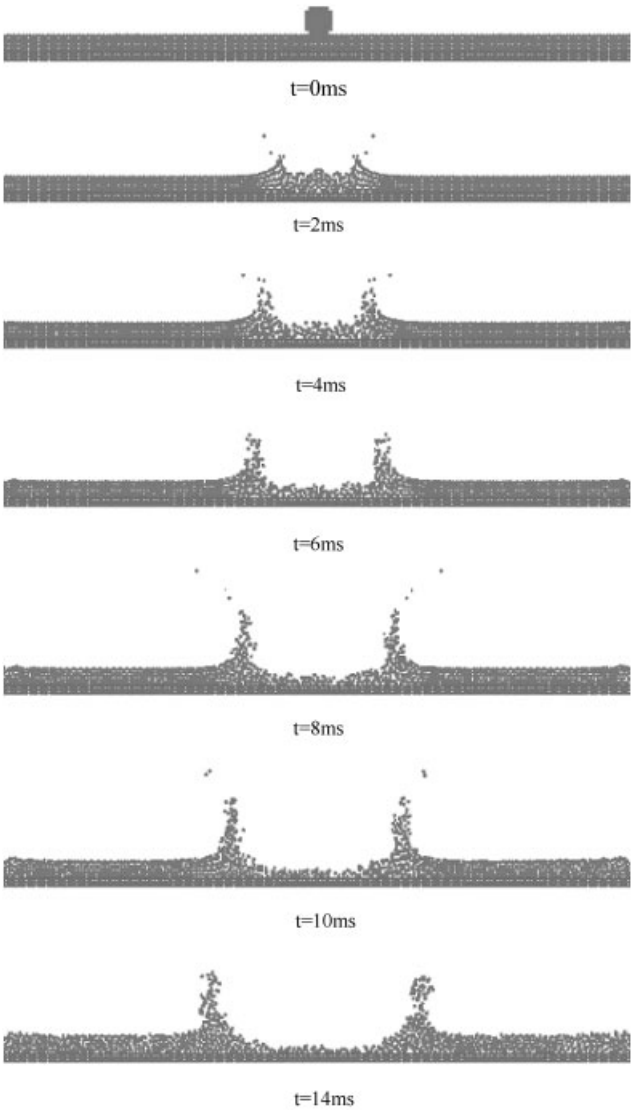

Figure 9. Calculated results of 2 mm liquid pool.

liquid film is very thin, a bowl-shaped thin crown is formed immediately after impact. The crown subsequently expands outward and breaks into many tiny droplets. The thickness of the liquid film behind the crown increases since the mass from the drop is more than that brought by the crown and the splashed droplets. When the thickness of the liquid film increases, the crown becomes normal to the film surface and propagates outward. The thickness of the film behind the crown is smaller than the initial one since the mass in this area is pushed to form the crown. It is also found that in this stage the radius of the crown can be described by a square function of time: $r_C = [c(t - t_0)]^{0.5}$ as seen in Weiss and Yarin's paper.

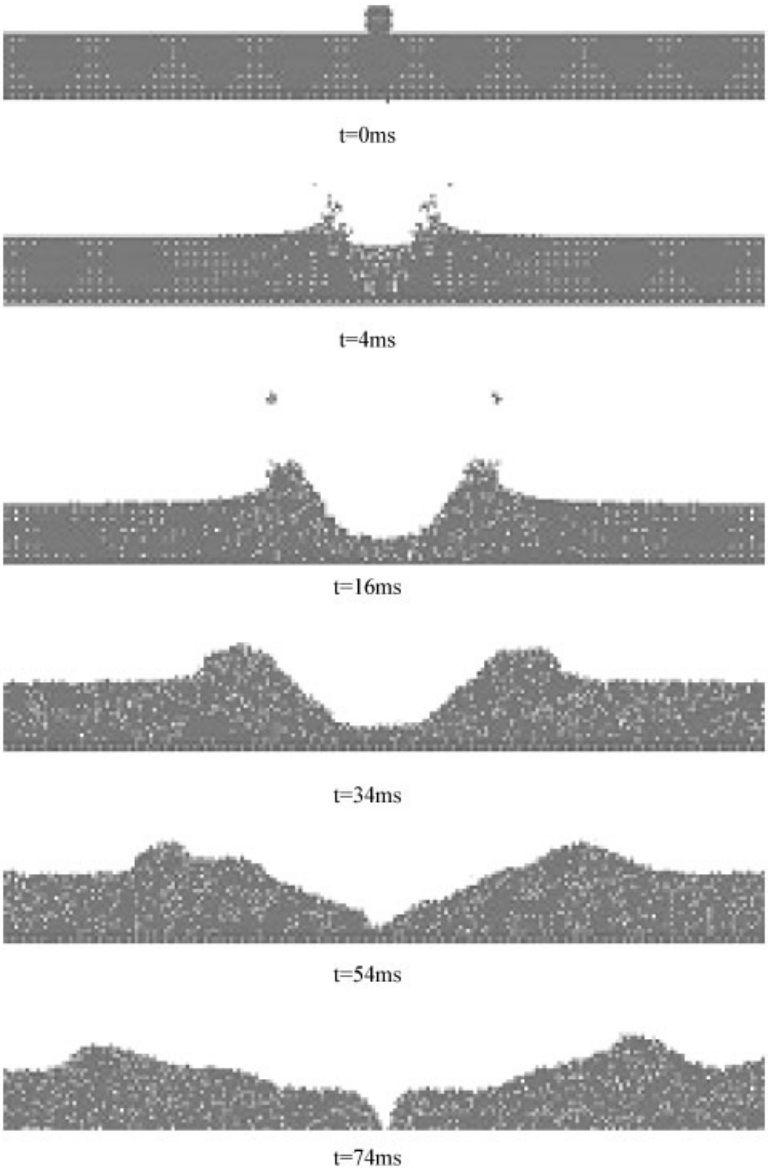

Figure 10. Calculated results of 7 mm liquid pool.

When the liquid film is thick enough, a crown and a deep cavity inside it are formed shortly after impact. The bottom of the cavity is initially oblate and then the base grows downward to form a sharp hole. The developing and recovering process of this sharp corner may be the main reason to the bubble entrainment and the rebounded jet observed in experimental results.

The further work is to study the impact dynamics under BWR condition in which the liquid film attached on the surface of the fuel rod is very thin and the mechanism of the impact on shallow liquid surface should be focused on.

REFERENCES

1. Guo YJ, Mishima K. A non-equilibrium mechanistic heat transfer model for post-dryout dispersed flow regime. *Experimental Thermal and Fluid Science* 2000; **26**:861–869.
2. Cokmez-Tuzla AF, Tuzla K, Chen JC. Characteristics of liquid-wall contact in post-CHF flow boiling. *International Journal of Heat and Mass Transfer* 2000; **43**:1925–1934.
3. Worthington AM. Impact with a liquid surface, studied by the aid of instantaneous photography. *Philosophical Transactions of the Royal Society of London* 1897; **A 189**:137–148.
4. Rein M. Phenomena of liquid drop impact on solid and liquid surfaces. *Fluid Dynamics Research* 1993; **12**:61–93.
5. Fukai J, Zhao Z, Poulikakos D. Modeling of the deformation of a liquid droplet impinging upon a flat surface. *Physics of Fluids* 1993; **A 5**:2588–2599.
6. Zhao Z, Poulikakos D, Fukai J. Heat transfer and fluid dynamics during the collision of a liquid droplet on a substrate—II. Experiments. *International Journal of Heat and Mass Transfer* 1996; **39**:2791–2802.
7. Kang BS, Lee DH. On the dynamic behavior of a liquid droplet impacting upon an inclined heated surface. *Experiment in Fluids* 2000; **29**:380–387.
8. Kim HY, Chun JM. Recoiling of liquid droplets upon collision with solid surfaces. *Physics of Fluids* 2001; **13**:643–659.
9. Šikalo Š, Marengo M, Tropea C, Ganic EN. Analysis of impact of droplets on horizontal surfaces. *Experimental Thermal and Fluid Science* 2002; **25**:503–510.
10. Zapalowicz Z. Critical contact Weber number for toluene droplets dropping onto the heated wall surface. *Experimental Thermal and Fluid Science* 2002; **25**:523–528.
11. Harlow FH, Welch JE. Numerical calculation of time-dependent viscous incompressible flow of fluid with free surface. *Physics of Fluids* 1965; **8**:2182–2189.
12. Trapaga G, Szekely J. Mathematical modeling of the isothermal impingement of liquid droplets in spray processes. *Metallurgical Transactions B* 1991; **22**:901–914.
13. Fukai J, Shiiba Y, Yamamoto Y *et al.* Wetting effects on the spreading of a liquid droplet colliding with a flat surface: experiment and modeling. *Physics of Fluids* 1995; **7**:236–247.
14. Yarin AL, Weiss DA. Impact of drops on solid surfaces: self-similar capillary waves, and splashing as a new type of kinematic discontinuity. *Journal of Fluid Mechanics* 1995; **283**:141–173.
15. Bussmann M, Chandra S, Mostaghimi DJ. Modeling the splash of a droplet impacting a solid surface. *Physics of Fluids* 2000; **12**:3121–3132.
16. Rein M. The transitional regime between coalescing and splashing drops. *Journal of Fluid Mechanics* 1996; **306**:145–165.
17. Liow JL. Splash formation by spherical drops. *Journal of Fluid Mechanics* 2001; **427**:73–105.
18. Weiss DA, Yarin AL. Single drop impact onto liquid films: neck distortion, jetting, tiny bubble entrainment, and crown formation. *Journal of Fluid Mechanics* 1999; **385**:229–254.
19. Hobbs PV, Osheroff T. Splashing of drops on shallow liquids. *Science* 1967; **158**:1184–1186.
20. Macklin WC, Hobbs PV. Subsurface phenomena and the splashing of drops on shallow liquids. *Science* 1969; **166**:107–108.
21. Wang AB, Chen ChCh. Splashing impact of a single drop onto very thin liquid films. *Physics of Fluids* 2000; **12**:2155–2158.
22. Manzello SL, Yang JC. An experimental study of a water droplet impinging on a liquid surface. *Experiments in Fluids* 2002; **32**:580–589.
23. Koshizuka S, Oka Y. Moving-particle semi-implicit method for fragmentation of incompressible fluid. *Nuclear Science and Engineering* 1996; **123**:421–434.
24. Koshizuka S, Oka Y. Numerical analysis of breaking waves using the moving particle semi-implicit method. *International Journal for Numerical Methods in Fluids* 1998; **26**:751–769.
25. Koshizuka S, Yoon HY, Yamashita D, Oka Y. Numerical analysis of natural convection in a square cavity using MPS-MAFL. *Computational Fluid Dynamics Journal* 2000; **8**:485–494.
26. Nomura K, Koshizuka S, Oka Y *et al.* Numerical analysis of droplet breakup behavior using particle method. *Journal of Nuclear Science and Technology* 2001; **38**:1057–1064.
27. Brackbill JU, Kothe DB, Zemach C. A continuum method for modeling surface tension. *Journal of Computational Physics* 1992; **100**:335–354.

